Friction Isolated Rotary System for High-Precision Roll-to-Roll Manufacturing

Dongwoo Kang[a], Xin Dong[b], Hyunchang Kim[a], Pyungwon Park[a], Chinedum E. Okwudire[b*]

[a]Department of Printed Electronics, Korea Institute of Machinery and Materials, Yuseong-gu, Daejeon, Korea

[b]Department of Mechanical Engineering, University of Michigan, 2350 Hayward Street, Ann Arbor, MI 48109, USA

[*]Corresponding author. Tel.: +1 734 647 1531; Fax.: +1 734 647 9379

E-mail address: okwudire@umich.edu (C. E. Okwudire)

Abstract

High precision roll-to-roll processes are believed to be one of the most promising technologies for manufacturing flexible and large-area thin film electronics. However, broadband frictional disturbances caused by the guiding ball bearings affect the precision of the processing roller in the roll-to-roll system, severely hampering the quality of the manufactured products. Conventional feedback control techniques encounter difficulties in mitigating the broadband frictional disturbances. This paper presents a novel rotary system for high-precision roll-to-roll manufacturing process. Friction isolator (FI), a robust and cost-effective mechatronics method, is implemented in the system to mitigate the undesirable effects of friction during continuous printing processes. Frequency domain analysis shows that the proposed rotary system with FI achieves significantly improved attenuation of frictional disturbance, compared to the case without it. A rotary FI is designed and optimized to minimize the adverse effects of bearing friction without overly sacrificing the high rigidity of the machine. A precision rotary system is then built using the designed FI prototype. Experiments carried out on the prototype friction-

isolated rotary system demonstrate up to 61% reduction in root-mean-square tracking error during constant velocity motion, compared to a conventional roll-to-roll system without FI.
Keywords: roll-to-roll manufacturing, friction, rotary bearing, tracking control, disturbance observer

1. Introduction

Roll-to-roll manufacturing processes, that pattern and coat electronic functional materials on plastic films, are considered as low-cost and high throughput technologies to manufacture flexible and large-area thin film electronics, such as organic photovoltaics, thin film transistors, light-emitting diodes, sensors and fuel cells [1]-[5]. In a typical roll-to-roll manufacturing system (see Figure 1), processes are carried out by transporting the plastic film continuously from unwinder to winder. For this purpose, the processing roller is generally controlled to move at constant velocity (CV) while tension of the plastic film is controlled by the unwinder and winder [6]. Precision (i.e., tracking accuracy) of the processing roller during CV motion is crucial to the performance of roll-to-roll system because the resulting positioning error directly affects the quality of the manufactured products. For example, successive print patterns are often aligned with the previously printed patterns on the film (also known as print registration) and tracking error of the processing roller during CV motions may cause position misalignment on the successive patterns in the film transport direction [7]. Therefore, registration requirement is very tight for printed electronics, on the order of a few micrometers [8].

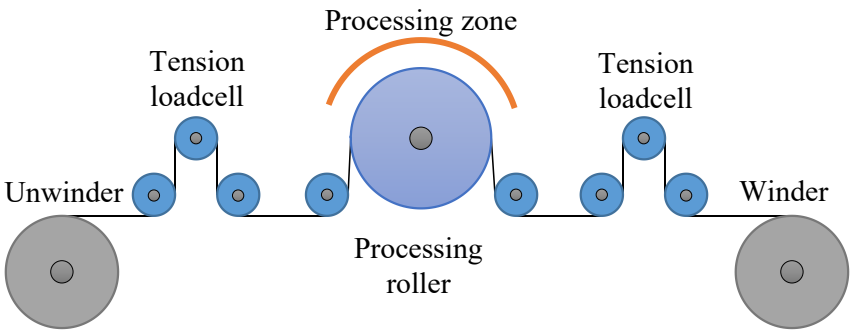

Figure 1. Schematic of a typical roll-to-roll manufacturing system.

During CV motions, tracking performance is mainly affected by two types of disturbances. The first one is position-dependent driving torque ripple caused by cogging forces, reluctance forces, unbalanced phase forces, phase misalignment and current offset from the servo motor [9]. Torque ripple occurs in a periodic manner with fundamental frequency determined by the pole pitch of the motor. As a result, the dominant peak of torque ripple can be effectively suppressed using force observer [10] and/or model-based compensation [11]. The other disturbance is caused by friction fluctuation as the balls of the guiding bearings roll inside the grooves [12]-[14]. There are only a few studies on mitigating the undesirable effects of friction fluctuations on the tracking performance of the system during CV motions. Armstrong [13] characterized the position-dependent friction disturbances in robotic joint and compensated the repeatable portions using a lookup table [13]. Miura et al. experimentally analyzed the friction fluctuations in several linear guideways and reported their detrimental effects on the smoothness of the motion [14]. They concluded that high frequency frictional disturbances can be reduced through design modifications, such as polishing the guideway and arranging the retained balls [14]. However, the remaining broadband disturbances (at low-to-medium frequency) still pose

significant challenges to the conventional servo controller, hampering the tracking performance of the system.

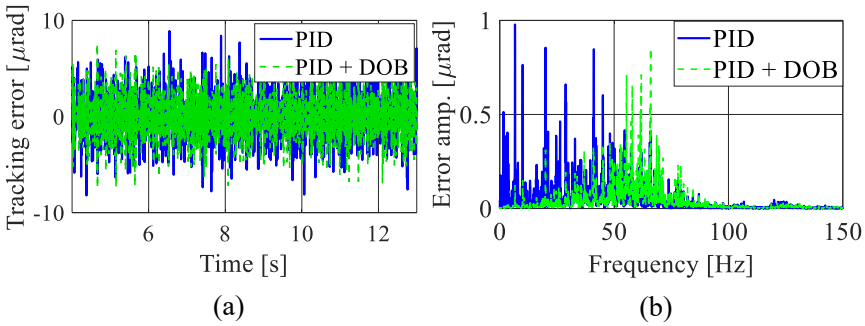

Figure 2. (a) Tracking errors of the processing roller during CV motion of 20 rpm, and (b) frequency spectra of the position error signals.

To illustrate the undesirable effects of friction fluctuations, experiments are carried out on a prototype roll-to-roll system whose design is further discussed in Section III. The processing roller is supported by double rows of ball-bearings. An industry standard PID controller is used to control the motion of the roller; it is tuned to a closed-loop bandwidth of 48 Hz. Figure 2 (a) shows the typical motion errors of the processing roller while it is moving at a CV of 20 rpm. The roller has a root-mean-square (RMS) tracking error of 2.44 μrad with the PID controller alone. As seen from the frequency spectra of the position error signals (see Figure 2 (b)), the system suffers from frictional disturbances at low-to-medium frequency regions. Disturbance observer (DOB) is often used to improve the disturbance rejection of the feedback controller beyond what is achievable with standard PID controller [15][16]. Therefore, an inverse-model-based DOB with a cutoff frequency of 100 Hz is implemented [15]-[17]. The RMS error is slightly reduced to 2.13 μrad when the DOB is introduced, as the disturbance at very low frequency region (< 30 Hz) is effectively suppressed. However, frictional disturbances

with frequency components between 30 Hz and 100 Hz are largely unaffected due to the limited bandwidth of DOB. Increasing gains of the servo controller (e.g., PID controller or DOB) often lead to stability and robustness issues which are detrimental to the performance of the system [18].

Friction isolator (FI), also known as compliant joint, is a robust and cost-effective mechatronics approach proposed by Dong et al. in [19] to address the undesirable effects of friction on linear nanopositioning (NP) stages with mechanical bearings. The idea of FI is to connect the mechanical bearings to a NP stage using a joint that is very compliant in the motion direction, thus, effectively isolating the stage from bearing friction. They have demonstrated that FI significantly reduces the settling times and quadrant glitches of NP stages with mechanical bearings during point-to-point motions and circular motions, respectively [19][20]. However, the influence of FI on the tracking performance of a NP stage during CV motions has not been explored; also, its applicability to rotary systems has not been demonstrated. Therefore, this paper focuses on investigating the benefits of FI on mitigating the effects of friction fluctuations on the precision of continuous roll-to-roll manufacturing systems, in particular, the processing roller.

The concept and dynamic model of the proposed friction-isolated rotary system are described in Section 2. The design of a rotary FI prototype is then outlined in Section 3. In Section 4, experiments are carried out on an in-house built rotary system with the designed FI prototype and the tracking performance of the proposed system during CV motions is evaluated. This is followed by conclusions and future work in Section 5.

2. Friction-isolated Rotary System

2.1. Concept

Figure 3 (a) shows the schematic of a conventional rotary system for roll-to-roll manufacturing. The processing roller of inertia I_p is guided by a pair of rotary ball bearings, each of inertia I_a. The viscous friction coefficient between the sliding surfaces of the bearings are denoted as c_f. Disturbances during constant velocity (CV) motions due to friction fluctuations are modeled as torques T_{f1} and T_{f2}; T_a and T_d are respectively the motor driving torque and other miscellaneous disturbances such as motor torque ripple and process induced disturbance. Figure 3 (b) shows the schematic of the proposed friction-isolated rotary system for high precision roll-to-roll manufacturing. Rather than being rigidly attached to the processing roller, the inner rings of the ball bearings are connected using friction isolators (FIs) of stiffness k and damping coefficient c. The isolators provide sufficient compliance in the motion direction (i.e., θ) while remaining stiff in other off-motion directions. Note that θ_p, θ_{a1} and θ_{a2} are the angular positions of the processing roller and two rotary bearings, respectively.

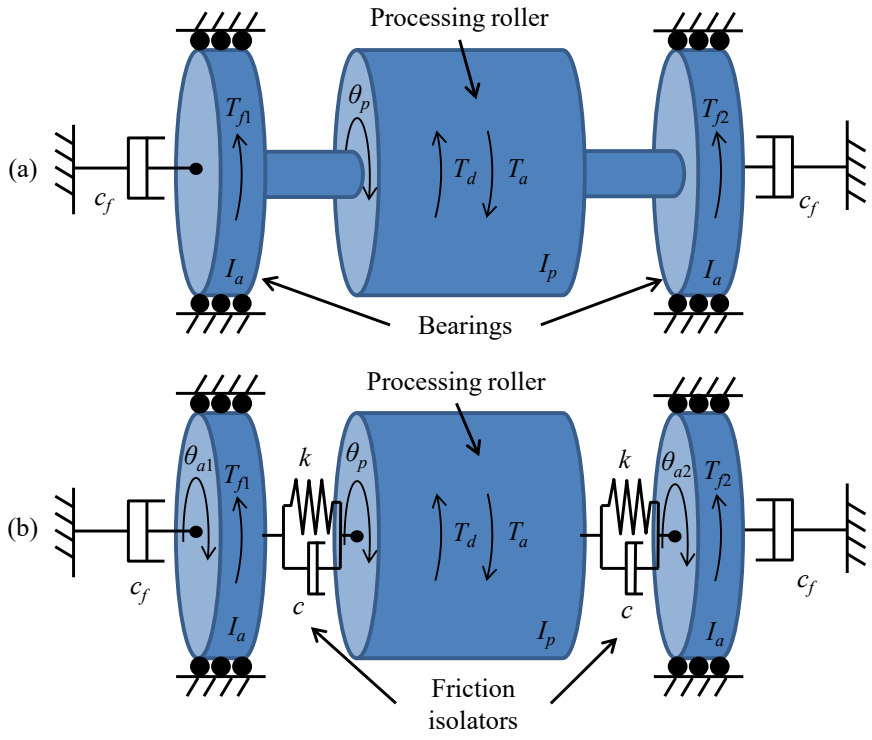

Figure 3. Schematic of (a) a conventional rotary system that is guided by ball bearings, and (b) proposed friction-isolated rotary system.

Assuming rigid body behavior, the plant dynamics (i.e., transfer function from motor driving torque to angular position of the processing roller) can be derived as [20]

$$G_{p,R} = \frac{1}{\left(I_p + 2I_a\right)s^2 + 2c_f s} \tag{1}$$

$$\begin{aligned} G_{p,FI} &= \frac{I_a s^2 + \left(c + c_f\right)s + k}{a_4 s^4 + a_3 s^3 + a_2 s^2 + a_1 s}; \\ a_4 &= I_p I_a; a_3 = c\left(I_p + 2I_a\right) + c_f I_p; \\ a_2 &= k\left(I_p + 2I_a\right) + 2cc_f; a_1 = 2kc_f \end{aligned} \tag{2}$$

where s is the Laplace variable, and subscripts R and FI denote the cases without and with FI, respectively. Similarly, the open loop transfer function from frictional disturbance to angular position of the roller (assuming $T_{f1} = T_{f2}$) can be obtained as [20]

$$D_{d,R} = 2G_{p,R} \tag{3}$$

$$D_{d,FI} = 2G_{p,FI}\frac{cs+k}{I_a s^2 + \left(c + c_f\right)s + k} \tag{4}$$

Observe that in a conventional rotary system, the frictional disturbance directly affects the stage dynamics, jeopardizing precision of the processing roller. In the proposed friction-isolated stage, the undesirable effects of friction fluctuations are mechanically low-pass filtered through the additional dynamics introduced by the FIs. However, note that high enough $c + c_f$ is needed to avoid large amplitude at the dominant resonance of the FIs. Large values of c reduce the low-pass filtering effect at frequency regions beyond the dominant resonance due to the presence of c in the numerator of $D_{d,FI}$. Therefore, it is more desirable to increase $c + c_f$ by increasing c_f. Note that though the proposed friction isolator acts in a manner similar to a classical vibration isolator [21], they are fundamentally different. The excitation source of a vibration isolator is exogenous, i.e., its amplitudes or frequencies do not depend on the states of the vibration isolator. However, the excitation source of a friction isolator (i.e., friction force) depends on the states of the friction isolator, often in a nonlinear manner [22][23].

2.2. Frequency Domain Analysis

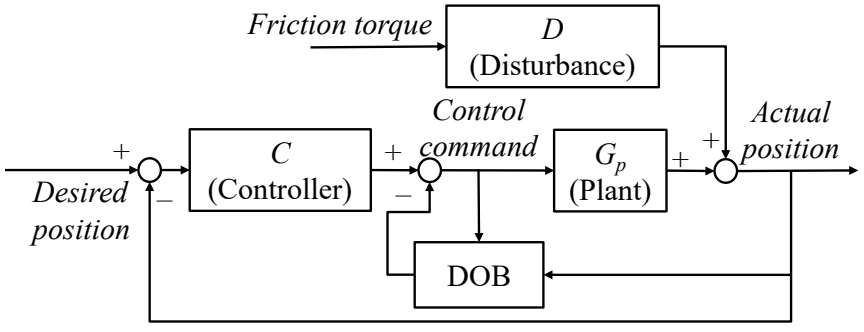

Figure 4. Control block diagram with feedback controller and DOB.

To further illustrate the benefits of FI in mitigating the undesirable effects of frictional disturbance, frequency domain analysis is carried out. As shown in Fig. 4, an industrial standard PID controller is used to control the motion of the processing roller; it is tuned to 100 Hz closed loop bandwidth. Since the feedback controller has limited ability in rejecting disturbances, an inverse-model-based disturbance observer (DOB) [16]-[18][20] is implemented to further attenuate the low frequency disturbances due to frictional variations; it is tuned to 80 Hz bandwidth. The closed loop transfer function from frictional disturbance to roller position is then obtained as [17]

$$G_{d,R} = \frac{D_R G_n \left(1-Q\right)}{Q\left(G_{p,R} - G_n\right) + G_n \left(1 + CG_{p,R}\right)}$$
$$G_{d,FI} = \frac{D_{FI} G_n \left(1-Q\right)}{Q\left(G_{p,FI} - G_n\right) + G_n \left(1 + CG_{p,FI}\right)} \tag{5}$$

where C is the feedback (PID) controller (the derivative action is low-pass filtered using a first order filter with time constant τ), Q is a low-pass filter to guarantee the stability of the DOB, and $G_n = G_{p,R}$ is the nominal plant model that describes the low-frequency characteristics of the conventional rotary system (dominated by rigid body dynamics). They are given by [20]

$$C = K_p + \frac{K_d s}{\tau s + 1} + \frac{K_i}{s} \tag{6}$$

$$Q = \frac{\left(2\pi f_Q\right)^2}{\left(s + 2\pi f_Q\right)^2} \tag{7}$$

Table 1. Parameters of the Rotary System.

Parameters	**Value**
I_p	0.15 kgm^2
I_a	0.015 kgm^2
K_p	1.54×10^4 N/rad
K_d	81.62 Ns/rad
K_i	6.16×10^5 N/rad·s
T_f	0.0005884 s
f_Q	80 Hz

Figure 5 (a) compares the magnitudes of $G_{d,R}$ and $G_{d,FI}$ using different stiffness k for FI. Note that a modal damping of 0.1% is introduced to account for the damping of the FI (i.e., c) and the remaining parameters are summarized in Table 1. Note that the parameters are obtained based on the friction-isolated rotary system whose design is discussed in Section 3. Observe that the frictional disturbance in the high frequency region is effectively suppressed by the FI, thanks to its low-pass filtering effect. The benefits of FI become more dominant when the stiffness is reduced since the magnitude of $G_{d,FI}$ rolls off after the resonance peak. In other words, a lower stiffness FI leads to better mitigation of frictional disturbance. Figure 5 (b) shows the influence of viscous friction (c_f) on the effectiveness of FI. Since the FI design often has limited damping [20], the resonance peak has very large amplitude if the frictional damping is small. This poses significant challenge since the dominant resonance can be easily excited (e.g., by friction variation), generating large position errors. Therefore, a high damping coefficient at the bearing location is necessary to attenuate the resonance peak and achieve the desired performance of FI.

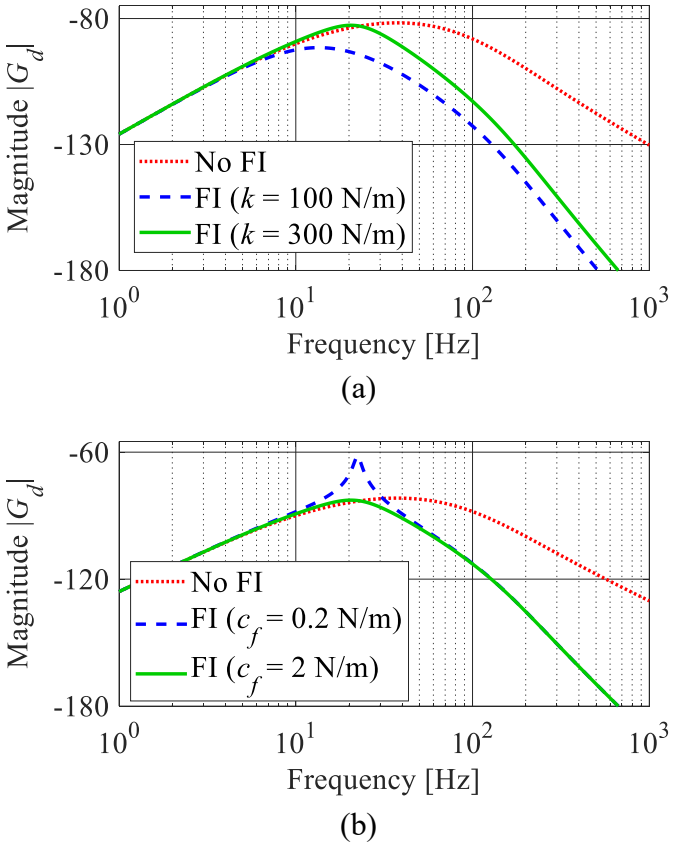

Figure 5. Magnitudes of $G_{d,R}$ and $G_{d,FI}$ with different (a) stiffness (c_f = 2 Nms/rad is used), and (b) viscous coefficient (k = 300 Nm/rad is used).

3. Design of Rotary System with FI

3.1. Overview of Design

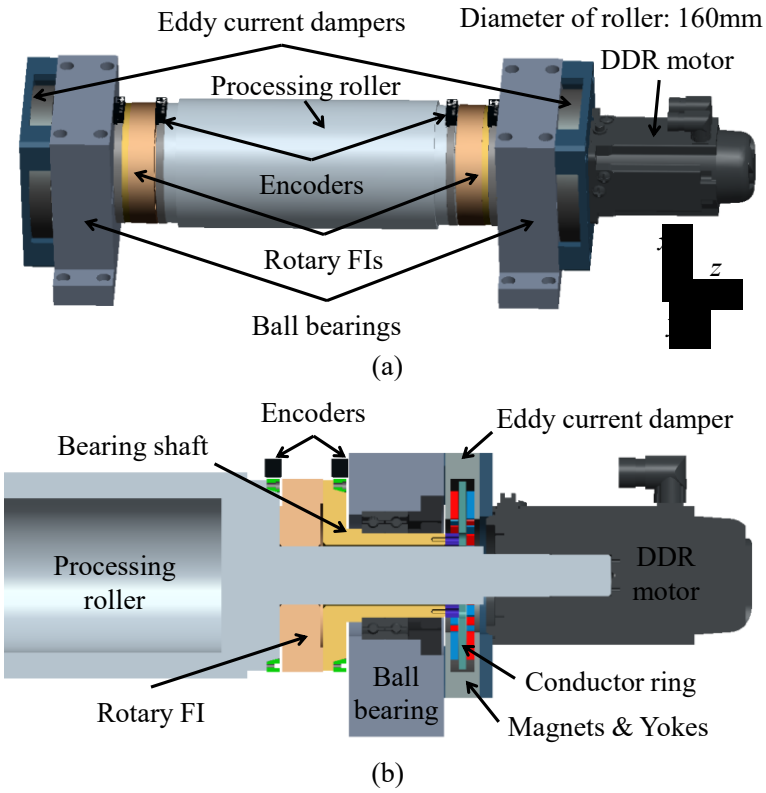

Figure 6. (a) CAD model, and (b) cross-sectional view of the prototype friction-isolated rotary system.

To validate the proposed method, a friction-isolated rotary system is designed – see Figure 6. The processing roller is guided by a pair of angular contact ball bearings (NSK, 7013A). A direct-drive rotary (DDR) motor (Kollmorgen, C042A) is used to drive the system. Rotary FIs, whose design is discussed in detail in the next section, are used to connect the processing roller to the inner rings of the rotary bearings. A rotary eddy current mechanism is implemented to achieve the desired viscous damping at the bearing location, as discussed in the next section.

3.2. *Design of Rotary Friction Isolator*

As shown in Figure 7, symmetric cartwheel flexure (SCF) mechanism [24] with four leaf springs are adopted for the FI; the center platform of the flexure is connected to the processing roller and the outer platform is connected to the inner ring of the ball bearing. The symmetric structure of SCF reduces drift of the rotation center during motion. In addition, the over-constrained flexure mechanism effectively improves rigidity in off-motion directions.

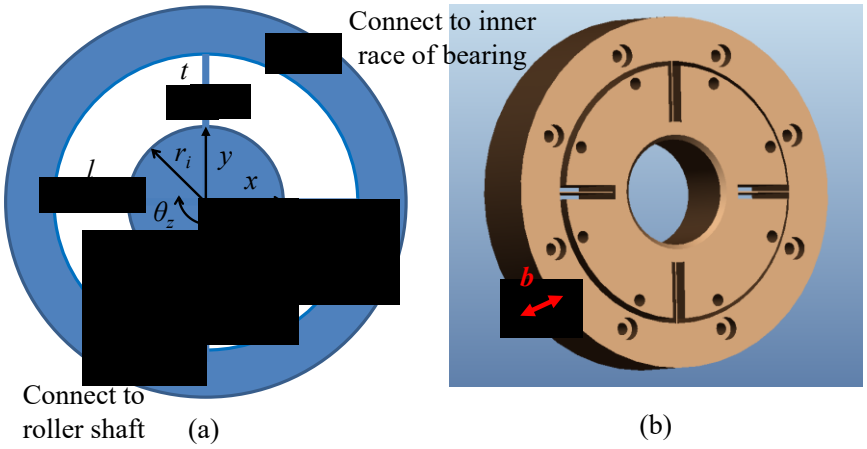

Figure 7. (a) Schematic, and (b) CAD drawing of SCF design.

To achieve the desired attenuation of frictional disturbance, the FI should have minimal stiffness in the motion direction (i.e., θ_z). In the meantime, it must maintain high stiffness in the off-motion directions (e.g., radial directions), so as not to overly sacrifice the rigidity of the ball bearing. Therefore, the parameters of the SCF mechanism, specifically, leaf length l, leaf thickness t, leaf width b, and outer platform radius r are optimized to maximize the stiffness ratios between off-motion directions and motion direction while satisfying other design

constraints (e.g., maximum stress and dimension). Let us denote K_{11}-K_{66} as the stiffness of the SCF in the x, y, z, θ_x, θ_y and θ_z directions; the objective can then be expressed as

$$\text{Maximize } K_{ii}/K_{66} \text{ where } i = 1,\ldots,5 \tag{8}$$

There are several constraints regarding the stiffness, stress and dimension limitations of the flexure mechanism. First of all, the axial and radial stiffness of the SCF should be of similar order of magnitude as the ball bearings so as not to overly sacrifice the rigidity of the system. Based on the approximated off-motion stiffness of ball bearings from the manufacture's (e.g., NSK) catalog, the following constraints are imposed to fulfill the stiffness requirements

$$K_{11}, K_{22} \text{ and } K_{33} \geq 120 \text{ N}/\mu\text{m} \tag{9}$$

Secondly, certain dimensional limitations are imposed on the design of SCF since it needs to fit into the designed rotary system. They are,

$$30 \text{ mm} \leq r_i < r \leq 60 \text{ mm (where } r_i = r - l) \tag{10}$$

$$0 < b \leq 30 \text{ mm} \tag{11}$$

$$0.5 \text{ mm} \leq t \leq l/10 \tag{12}$$

Eq. (10) indicates that the center and outer platforms of SCF should have large enough radius to prevent excessive deformation under loading. Note that the overall radius of the processing roller is set to 80 mm such that a sample length of 500 mm can be processed by a single turn. Furthermore, in Eq. (11), the width of the flexure mechanism is constrained to limit the overall length of the drive shaft and prevent low torsional stiffness. Finally, the thickness of the flexure leaf is constrained to avoid manufacturing issues while maintaining thin beam assumption.

To facilitate the design optimization, the stiffness of SCF is derived analytically

$$\begin{bmatrix} F_x & F_y & F_z & M_x & M_y & M_z \end{bmatrix}^T = \boldsymbol{K} \begin{bmatrix} x & y & z & \theta_x & \theta_y & \theta_z \end{bmatrix}^T \tag{13}$$

$$\boldsymbol{K} = \begin{bmatrix} K_{11} & \cdots & K \\ \vdots & \ddots & \vdots \\ K_{61} & \cdots & K \end{bmatrix} \tag{14}$$

where $[x\ y\ z\ \theta_x\ \theta_y\ \theta_z]^T$ is the 6-DOF deformation of the flexure and $[F_x\ F_y\ F_z\ M_x\ M_y\ M_z]^T$ is the external force and moment vector. Without loss of generality, the SCF can be treated as the flexure mechanism where a single moving platform (i.e., outer ring) is connected through several leaf-springs to the ground. Following the modeling technique discussed in [25], elastic potential energy stored in leaf-springs due to the motion of moving platform is modeled first. Then the stiffness matrix is calculated by applying Lagrange's equation to the elastic potential energy. Note that the nonlinear stiffening effect of the over-constrained flexure is ignored in this model for simplicity and the off-diagonal terms in the stiffness matrix become zero thanks to the symmetric structure of the SCF. The remaining diagonal terms are given by

$$K_{11} = K_{22} \approx 2\alpha\beta El \tag{15}$$

$$K_{33} \approx \frac{4\alpha\beta^3 El}{B} \tag{16}$$

$$K_{44} = K_{55} \approx \frac{\alpha\beta^3 El^3}{6}\left(1+\frac{2\xi-1}{B}\right) \tag{17}$$

$$K_{66} \approx \frac{2\alpha^3\beta\xi El^3}{3} \tag{18}$$

where E is the Young's modulus, υ is the Poisson's ratio and the non-dimensional parameters are described as follows

$$\alpha = \frac{t}{l};\ \beta = \frac{b}{l};\ \gamma = \frac{r}{l};\ \gamma_i = \frac{r_i}{l};\ \xi = 2+6\gamma(\gamma-1) = 2+6\gamma_i(\gamma_i+1);\ B = 1+\frac{12\beta^2(1+\upsilon)}{5} \tag{19}$$

The stiffness ratios of off-motion directions over motion direction can then be calculated as

$$\frac{K_{11}}{K_{66}} = \frac{K_{22}}{K_{66}} \approx \frac{3}{\alpha^2 l^2 \xi} \tag{20}$$

$$\frac{K_{33}}{K_{66}} \approx \frac{6\beta^2}{\alpha^2 l^2 \xi B} \tag{21}$$

$$\frac{K_{44}}{K_{66}} = \frac{K_{55}}{K_{66}} \approx \frac{\beta^2}{4\alpha^2 \xi}\left(1 + \frac{2\xi - 1}{B}\right) \tag{22}$$

Before stepping into detailed optimization, sensitivity analysis is carried out to illustrate the effects of different design parameters on the objective. Observe from Eq. (13) – (16) and (18) – (20) that increasing β always leads to higher off-motion stiffness as well as higher stiffness ratios between $K_{33} – K_{55}$ and K_{66}. This indicates that β should be set to its upper limit. Therefore, b = 30 mm is used to achieve the largest possible β given a fixed l. Similarly, as ξ decreases, the stiffness ratios are increased without affecting the off-motion stiffness $K_{11} – K_{33}$. Since ξ monotonically increases for γ_i (or r_i) > 0, r_i is set to its lower limit of 30 mm to minimize ξ. As a result, the design problem is simplified to find the optimal parameters for l and α.

Figure 8 shows the calculated stiffness ratio of K_{11} (and K_{22}) over K_{66} as a function of α and l. Observe that reducing α leads monotonically increased stiffness ratio at a fixed l. Therefore, t should be set to its lower limit of 0.5 mm to achieve a minimum α. Although a larger l generally enables the choice of a lower α, thus, higher stiffness ratio, it cannot be arbitrary increased due to the existence of other design constraints. By plotting the active geometry and stiffness constraints from Eq. (9) – (12), the stiffness ratio of K_{11} (and K_{22}) over K_{66} is maximized at a leaf length (l) of 26 mm (highlighted by the red circle in Fig. 8). Similar behavior is observed for other stiffness ratios and exactly the same optimal parameters are obtained for α and l – see Table 2.

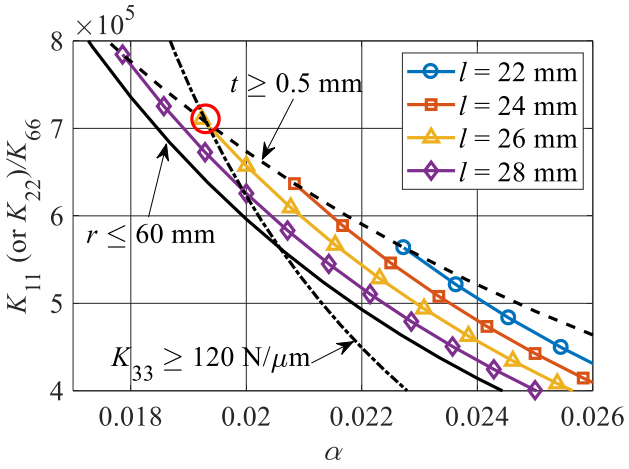

Figure 8. Calculated stiffness ratio K_{11} (and K_{22}) over K_{66} using different α and l.

Table 2. Optimal Parameters of Designed FI

Parameters	**Value**
l	26 mm
b	30 mm
t	0.5 mm
r	56 mm

Table 3. Comparison of SCF Stiffness Using Analytical Model and FE Simulation

Stiffness	**Analytical**	**FEM**	**Difference**
K_{11}, K_{22} N/μm	230.85	210.17	9.84 %
K_{33} N/μm	119.32	110.72	7.77 %
K_{44}, K_{55} Nm/mrad	127.63	118.39	7.80 %
K_{66} Nm/rad	324.85	331.76	-2.08 %

Since the design parameters are optimized using analytical approximations, the accuracy of the model is validated using finite element (FE) simulation with Pro/Engineer®. Table 3 compares the stiffness parameters obtained from analytical model and FE simulation. The model is fairly accurate in estimating the stiffness in all directions as the maximum deviation is less than 10%.

3.3. Design of Eddy-current Damper

It is observed from the frequency domain analysis in Section 2 that a larger viscous coefficient c_f is desired for attenuating the resonance peak due to the introduction of FI. However, this is associated with increased torque which may cause yield or structural failure of the SCF mechanism. The total torque experienced by the SCF is given by

$$T_{max} \geq I_a a_{max} + c_f \omega_{max} + T_{Bearing} \tag{23}$$

where ω_{max} and α_{max} are the maximum angular velocity and acceleration of the processing roller, and $T_{bearing}$ is the Coulomb friction torque of the ball bearing (0.7 Nm for each side of bearing). In this study, ω_{max} is set to 10 rpm (corresponds to a roll-to-roll process at 5 m/min) and a_{max} is set to $10\omega_{max}$. The maximum allowable torque (T_{max}) that SCF can withstand at its maximum rotary angle can be derived as

$$T_{max} = K_{66}\theta_{\max} \leq \frac{2l^3\alpha^2\beta\xi}{3(3\gamma-1)} \cdot \frac{\sigma_Y}{S_f} \tag{24}$$

The maximum moment at the leaf spring of the SCF is obtained from the beam bending theory and the free-body diagram assuming the SCF undergoes certain rotary angle. The maximum rotary angle of the SCF is determined by limiting the maximum moment at leaf spring under the material yield strength. Considering the yield strength (i.e., σ_Y) of SUS304 (215 MPa) and a safety factor (S_f) of 1.5, T_{max} is calculated as 2.22 Nm. Combining it with experimentally identified bearing inertia and friction torque, the maximum viscous coefficient c_f is obtained as

1.3 Nms/rad. Given that the viscous damping of bearing friction is roughly 0.3 Nms/rad, the designed eddy current damper should provide an additional damping of 1 Nms/rad.

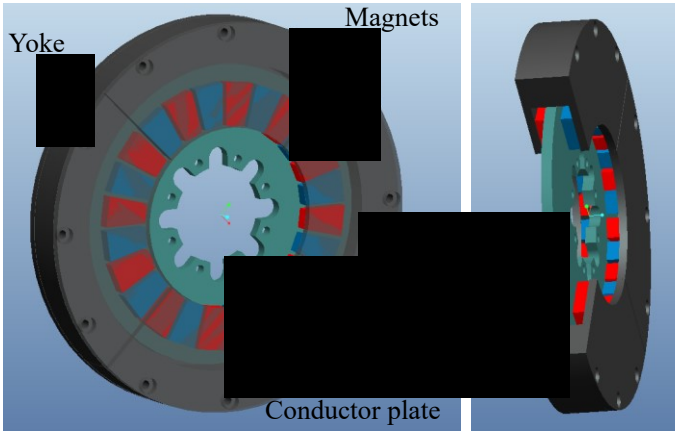

Figure 9. CAD model of the designed eddy current damper.

In the designed rotary eddy current mechanism (see Figure 9), the permanent magnets are arranged in the circumferential direction, which is similar to that of a doubled-sided linear motor. The rotating disc is placed between the upper and lower magnetic arrays and viscous damping torque is achieved due to the interaction of eddy current and magnetic field. The resulting damping torque (T_{damp}) can be obtained using ANSYS®. The material for permanent magnets is NdFe35, and the yoke and conductor plate are made of 1010 steel and C10100 Cu alloy, respectively. In order to achieve the desired damping coefficient of 1 Nms/rad, the radius and thickness of the conductor plate are selected respectively as 73 mm and 4.5 mm. The inner and outer radius of the yoke are designed as 44 mm and 95 mm. The thickness of the yoke and magnet are 4 mm and 6 mm, respectively.

4. Experimental Validation of Rotary FI System

As shown in Figure 10 (a), a rotary system equipped with the FI prototype is manufactured and assembled. The DDR motor is powered using a PWM amplifier (Kollmorgen, AKD-B00606). The angular position of the processing roller is measured using a ring encoder (Renishaw, encoder head – RGH20Y, ring scale – PESR20USA150) that is mounted on the side surface of the roller; it has an angular resolution of 1.33 μrad. The feedback controller is implemented using a real-time control board (dSPACE, DS1005) running at 100 μs cycle time and the angular position errors are down-sampled at 1 kHz sampling frequency. The motion stiffness of the fabricated SCF mechanism is tested using modal analysis. As seen from Figure 10 (b), the inner platform of SCF is fixed to the ground and an impact hammer is used to hit its outer platform in the motion direction. The circumferential displacement of the outer platform is measured by a capacitive sensor and the first (dominant) resonance mode is measured as 28.76 Hz (see Fig. 10 (c)). Combining this with the moving inertia (i.e., 0.011 kgm^2), the stiffness of SCF in the motion direction is calculated as 359.20 Nm/rad, which is very close to the designed value (10.6% deviation). The total viscous damping of the system for both sides of bearings and eddy current dampers is measured as 2.44 Nms/rad by moving the roller at CV motions and fitting the slope of the motor driving torques to the operating speeds.

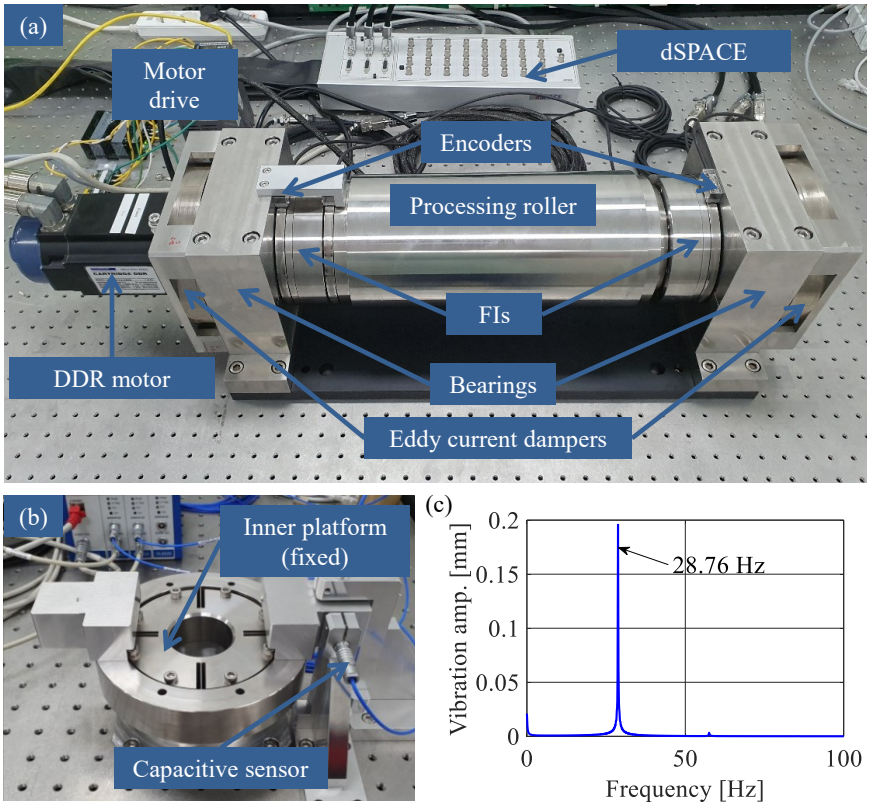

Figure 10. (a) In-house built prototype roll-to-roll system equipped with the designed FI, (b) experimental setup for modal analysis, and (c) measured dominant resonance mode of FI.

The performance of the designed friction-isolated system (i.e., FI case) is evaluated in experiments using constant velocity (CV) tracking test. The No FI case (i.e., a conventional rotary system) is achieved by swapping the designed FI with a rigid cylinder of the same rotating inertia. A PID controller is used for feedback control of the processing roller, it is tuned to 48 Hz closed loop bandwidth based on conventional loop-shaping approach. As discussed in Section II, an inverse-model-based disturbance observer is also implemented to attenuate the low frequency disturbances. The parameters of the nominal plant model is obtained through least-squares-fitting the low-frequency portion of the measured plant dynamics [15][20] and the cutoff frequency of the Q filter (i.e., low-pass filter in Eq. (7)) is tuned based on robust stability theory [15]. It is

observed that the introduction of FI mitigates the model uncertainties due to nonlinear friction dynamics at high frequency regions, enabling the use of Q filter with a cutoff frequency of 200 Hz while the No FI case is unstable when the cut-off frequency of Q filter is greater than 100 Hz. Similar behaviors are observed in a linear nanopositioning stage equipped with FIs [20].

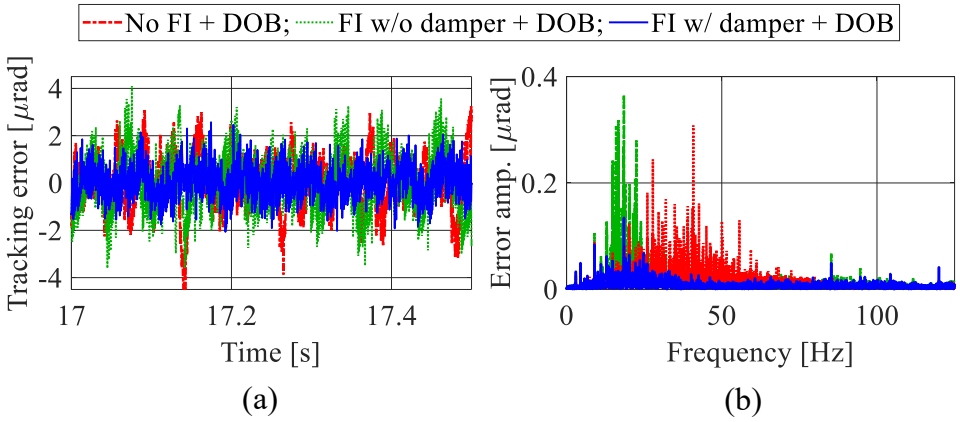

Figure 11. (a) Typical tracking errors during CV motion of 9 rpm, and (b) frequency spectra of the position error signals. Note that DOB with 100 Hz bandwidth is used in all cases.

Figure 11 (a) shows the typical tracking error of the in-house built rotary system when the processing roller is moving at a CV motion of 9 rpm and Table 4 summarizes the calculated RMS error. To demonstrate the importance of damping, the FI case without eddy current damper is also tested. In the presence of the DOB, the RMS tracking error of the No FI case is reduced from 1.82 μrad (i.e., achieved using the PID controller alone) to 0.95 μrad. Observe that DOB is not effective in mitigating the disturbances with frequency components of 30 – 100 Hz as seen from Figure 11 11 (b). On the other hand, using the friction-isolated system (without eddy current damper) with the same PID controller and DOB, the low-to-medium frequency disturbance is effectively attenuated, thanks to the low-pass filtering effect of the FI. However,

due to the low damping characteristics of the designed FI, the disturbance amplitudes near the dominant resonance mode are increased significantly, leading to an RMS error of 1.04 μrad which is even worse than the No FI case. When the designed eddy current damper is installed on the friction-isolated system, the disturbance around the resonance frequency of FI is effectively attenuated, resulting in an RMS tracking error of 0.46 μrad (52 % reduction relative to the No FI case). The error is further reduced to 0.37 μrad when the cutoff frequency of the DOB is increased to 200 Hz (which is unstable for the No FI case).

Table 4. Summary of RMS Tracking Errors During CV Motion of 9 rpm.

Test case	**RMS tracking error**
No FI	1.82 μrad
No FI + DOB (100 Hz)	0.95 μrad
FI w/o damper + DOB (100 Hz)	1.04 μrad
FI w/ damper + DOB (100 Hz)	0.46 μrad
FI w/ damper + DOB (200 Hz)	0.37 μrad

Figure 12 compares the RMS tracking errors of the No FI and FI case when the processing roller is moving at different levels of CV. At low speed, the system with FI shows similar tracking errors as the system without FI since the frictional disturbance mainly contains low frequency components that are below the dominant resonance of FI. As the velocity increases, the frictional disturbance shifts to higher frequency regions, leading to significantly increased tracking errors for the No FI case. This is because a conventional rotary system solely relies on servo controller (i.e., PID controller and DOB) for disturbance attenuation, which has

limited ability for mitigating these medium frequency disturbances. However, the introduction of FI greatly attenuates the frictional disturbance with frequency components above its dominant resonance, making it much easier for a DOB of the same bandwidth to suppress the remaining low frequency disturbance. As a result, the tracking error of the FI case at high speed motion is significantly smaller than that of the No FI case. In addition, the introduction of FI enables the use of a DOB with much higher bandwidth, leading to up to 61% reduction in RMS error when compared to the case without FI. The tracking performance of the friction-isolated system also remains largely unchanged as the speed of the processing roller varies, indicating that the proposed method is very robust.

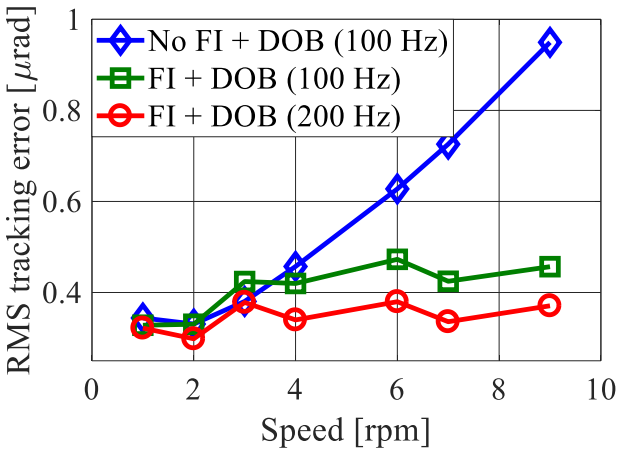

Figure 12. Comparison of tracking errors during CV motions of different speed; note that eddy current damper is installed in the FI case.

5. Conclusions and Future Work

In this paper, a novel rotary servo system for achieving high precision continuous roll-to-roll manufacturing has been presented. The proposed system integrates friction isolator (FI), a

mechanical component, to mitigate the undesirable effects of friction on the tracking performance of the processing roller during constant velocity motions, thus improving the quality of the manufactured products. It has been demonstrated through frequency domain analysis that FI improves the disturbance rejection ability of the system by low-pass filtering the frictional disturbance of the supporting bearings. A rotary FI prototype has then been designed using symmetric cartwheel flexure mechanism; its parameters have been optimized to achieve lowest stiffness in the motion direction (for better disturbance suppression) while maintaining high stiffness in off-motion directions so as not to unduly sacrifice the rigidity of the machine. An eddy current damper has also been designed to provide additional viscous damping that is critical for avoiding excessive vibrations at the dominant resonance of the FI. It has been demonstrated in experiments that the friction-isolated rotary system achieves up to 61% reductions in RMS tracking error during CV motions of different speed, compared to a conventional rotary system. Future work will combine the proposed friction-isolated rotary system with advanced control algorithms, such as iterative learning control, to further improve the tracking accuracy during CV motion.

Acknowledgements

This work is supported by Korea Institute of Machinery and Materials (KIMM) through the Government-funded Research Program (Grant NK224E): Precision/High-throughput roll-to-roll manufacturing system with real-time overlay compensation for flexible smart electronics and by National Science Foundation (NSF) Award (CMMI #1855354): Towards a Fundamental Understanding of a Simple, Effective and Robust Approach for Mitigating Friction in Nanopositioning Stages.

References

[1] Steenberg T, Hjuler HA, Terkelsen C, Sánchez MT, Cleemann LN, Krebs FC. Roll-to-roll coated PBI membranes for high temperature PEM fuel cells. Energy & Environmental Science 2012; 5(3): 6076-80.

[2] Sandström A, Dam HF, Krebs FC, Edman L. Ambient fabrication of flexible and large-area organic light-emitting devices using slot-die coating. Nature Communications 2012; 3(1): 1-5.

[3] Choi YM, Kang D, Lim S, Lee MG, Lee SH. High-precision printing force control system for roll-to-roll manufacturing. IEEE/ASME Transactions on Mechatronics 2017; 22(5): 2351-8.

[4] Krebs FC. Fabrication and processing of polymer solar cells: A review of printing and coating techniques. Solar Energy Materials and Solar Cells 2009; 93(4): 394-412.

[5] Du X, Hardt D, Anthony B. Real-time imaging of invisible micron-scale monolayer patterns on a moving web using condensation figures. IEEE Transactions on Industrial Electronics 2019; 67(5): 4077-87.

[6] Kim SK, Ahn CK. Self-tuning nonlinear control system design for roll-to-roll printing systems. IEEE/ASME Transactions on Mechatronics 2020.

[7] Seshadri A, Pagilla PR, Lynch JE. Modeling print registration in roll-to-roll printing presses. Journal of Dynamic Systems, Measurement, and Control. 2013; 135(3).

[8] Bartzsch M, Fuegmann U, Fischer T, Hahn U, Kempa H, Preissler K, Schmidt G, Huebler A. All-printed electronics and its applications: a status report. In NIP & Digital Fabrication Conference 2006; 2006(3): 13-6.

[9] Bascetta L, Rocco P, Magnani G. Force ripple compensation in linear motors based on closed-loop position-dependent identification. IEEE/ASME Transactions on Mechatronics 2009; 15(3): 349-59.

[10] Hwang TS, Seok JK. Observer-based ripple force compensation for linear hybrid stepping motor drives. IEEE Transactions on Industrial Electronics 2007; 54(5): 2417-24.

[11] Huang G, She J, Fukushima EF, Zhang C, He J. Robust reconstruction of current sensor faults for pmsm drives in the presence of disturbances. IEEE/ASME Transactions on Mechatronics 2019; 24(6): 2919-30.

[12] Fujita T, Matsubara A, Yamazaki K. Experimental characterization of disturbance force in a linear drive system with high-precision rolling guideways. International Journal of Machine Tools and Manufacture 2011; 51(2): 104-11.

[13] B. S. Armstrong BS. Dynamics for robot control: friction modelling and ensuring excitation during parameter identification. Ph.D. dissertation, Dept. Comp. Sci., Stanford Univ., Stanford, CA, USA, 1988.

[14] Miura T, Matsubara A, Yamaji I, Hoshide K. Measurement and analysis of friction fluctuations in linear guideways. CIRP Annals – Manufacturing Technology 2018; 67(1): 393-6.

[15] Jamaludin Z, Van Brussel H, Swevers J. Friction compensation of an xy feed table using friction-model-based feedforward and an inverse-model-based disturbance observer. IEEE Transactions on Industrial Electronics 2009; 56(10): 3848-53.

[16] Chen CS, Chen SK, Chen LY. Disturbance observer-based modeling and parameter identification for synchronous dual-drive ball screw gantry stage. IEEE/ASME Transactions on Mechatronics. 2019; 24(6): 2839-49.

[17] Schrijver E, Van Dijk J. Disturbance observers for rigid mechanical systems: equivalence, stability, and design. Journal of Dynamic Systems, Measurement, and Control 2002; 124(4): 539-48.

[18] Kim T, Yoo S, Seo T, Kim HS, Kim J. Design and force-tracking impedance control of 2-dof wall-cleaning manipulator via disturbance observer. IEEE/ASME Transactions on Mechatronics 2020; 25(3): 1487-98.

[19] Dong X, Liu X, Yoon D, Okwudire CE. Simple and robust feedforward compensation of quadrant glitches using a compliant joint. CIRP Annals – Manufacturing Technology 2017; 66(1): 353-6.

[20] Dong X, Okwudire CE. An experimental investigation of the effects of the compliant joint method on feedback compensation of pre-sliding/pre-rolling friction. Precision Engineering 2018; 54: 81-90.

[21] DeBra DB. Vibration isolation of precision machine tools and instruments. CIRP Annals – Manufacturing Technology 1992; 41(2): 711-8.

[22] Dong X, Okwudire C, Wang J, Barry O. On the friction isolator for precision motion control and its dynamics. In International Design Engineering Technical Conferences and Computers and Information in Engineering Conference 2019; 1: 1-10.

[23] Huang S, Liang W, Tan KK. Intelligent friction compensation: a review. IEEE/ASME Transactions on Mechatronics 2019; 24(4): 1763-74.

[24] Kim K, Ahn D, Gweon D. Optimal design of a 1-rotational dof flexure joint for a 3-dof h-type stage. Mechatronics 2012; 22(1): 24-32.

[25] Kang D, Gweon D. Analysis and design of a cartwheel-type flexure hinge. Precision Engineering 2013; 37(1): 33-43.